

See discussions, stats, and author profiles for this publication at: <https://www.researchgate.net/publication/9002031>

# Template burning inside TS-1 and Fe-MFI molecular sieves: an in situ XRPD study.

ARTICLE in JOURNAL OF THE AMERICAN CHEMICAL SOCIETY · DECEMBER 2003

Impact Factor: 12.11 · DOI: 10.1021/ja037229+ · Source: PubMed

CITATIONS

47

READS

27

5 AUTHORS, INCLUDING:



**Marco Milanesio**

Amedeo Avogadro University of Eastern Pied...

**113** PUBLICATIONS **947** CITATIONS

SEE PROFILE



**Gilberto Artioli**

University of Padova

**252** PUBLICATIONS **3,314** CITATIONS

SEE PROFILE



**Carlo Lamberti**

Università degli Studi di Torino

**378** PUBLICATIONS **12,760** CITATIONS

SEE PROFILE

## Template Burning inside TS-1 and Fe-MFI Molecular Sieves: An in Situ XRPD Study

Marco Milanese,<sup>†</sup> Gilberto Artioli,<sup>‡</sup> Alessandro F. Gualtieri,<sup>§</sup> Luca Palin,<sup>||,⊥</sup> and  
Carlo Lamberti<sup>\*,||</sup>

*Contribution from the Dipartimento di Scienze e Tecnologie Avanzate, Università del Piemonte Orientale "A. Avogadro", Corso T. Borsalino 54, I-15100 Alessandria, Italy; Dipartimento di Scienze della Terra, Università di Milano, Via Botticelli 23, I-20133 Milano, Italy; Dipartimento di Scienze della Terra, Università di Modena e R.E., Via S. Eufemia 19, I-41100 Modena, Italy; and Dipartimento di Chimica IFM, Università di Torino and INFN U.d.R. di Torino Università, Via P. Giuria 7, I-10125 Torino, Italy*

Received July 11, 2003; E-mail: carlo.lamberti@unito.it

**Abstract:** The high X-ray flux available at the European Synchrotron Radiation Facility (ESRF), combined with the use of a suitably designed area detector setup, allowed us to follow in real time the structural changes occurring during the template burning processes inside TS-1 and Fe-silicalite **MFI** zeolites with a X-ray powder diffraction technique (XRPD). Rietveld analysis of the XRPD patterns collected in the 350–1000 K interval, integrated each 15 K, yields to the determination of the template overall occupancy factor versus  $T$  with an accuracy comparable with that obtained by thermogravimetric measurements, routinely employed for this purpose. The evolution of the structural parameters ( $V$ ,  $a$ ,  $b$ ,  $c$ , site occupancy factor of the template molecule) vs  $T$  has been obtained. These data allow us to have, for the first time, a complete view of the structural rearrangements induced by the template burning process on the zeolitic framework. The differences caused by the different heteroatom inserted in the **MFI** lattice (Ti or Fe) are discussed. For both TS-1 and Fe-**MFI**, the kinetics of the reaction were investigated, to obtain the activation energy of the calcinations process employing the nonisothermal data according to the theory recently proposed by Kennedy and Clark [*Thermochim. Acta*, **1997**, *307*, 27–35]. For TS-1 only, the time-resolved template burning experiment has been repeated in isothermal conditions at four different temperatures, to obtain the activation energy from isothermal data, according to the standard procedure. Comparison between Arrhenius plots obtained from isothermal and nonisothermal data demonstrates that the Kennedy and Clark method can be also applied to complex materials such as the **MFI** zeolites. This approach, when applied to time-resolved XRPD studies, is much less time consuming (requesting, in principle, one single nonisothermal run) with respect to the classic approach, which requests at least three isothermal runs. Moreover, it allows a remarkably lower associated error ( $151 \pm 11$  versus  $146 \pm 30$  kJ mol<sup>-1</sup>) due to the much higher number of experimental points employed to perform the linear fit.

### Introduction

The **MFI** framework<sup>1</sup> shows a two-dimensional pore system consisting of two intersecting sets of tubular channels,<sup>2,3</sup> a linear one parallel to the [010] direction, with an opening of approximately  $5.4 \times 5.6$  Å<sup>2</sup>, and a sinusoidal one parallel to the [100] direction, with an opening of  $5.1 \times 5.5$  Å<sup>2</sup>. Both channels are defined by 10-member rings of SiO<sub>4</sub> tetrahedra. **MFI**-type

zeolites (zeotype) materials are among the most important microporous solid for their large use in the field of catalysis and fine chemistry. The most used **MFI** material is ZSM-5 zeolite, first synthesized in the Mobil laboratories in the late 1970s.<sup>2</sup> The isomorphous substitution of Si by other tetrahedrally coordinated heteroatoms (different from Al<sup>III</sup>) such as Ti<sup>IV</sup> or Fe<sup>III</sup> in small amounts (up to 2–3% in weight) provides new materials, named as titanium silicalite-1<sup>4</sup> and Fe-silicalite,<sup>5</sup> respectively (more briefly TS-1 and Fe-**MFI**), showing specific catalytic properties in oxidation and hydroxylation reactions, related to the coordination state of the heteroatom.<sup>6</sup> The **MFI** framework can be synthesized also in the totally siliceous form, resulting in silicalite-1 material.<sup>7,8</sup> Finally, the recent discovery of an Al containing natural zeolite (mutinaite) with the **MFI**

<sup>†</sup> Università del Piemonte Orientale "A. Avogadro".

<sup>‡</sup> Università di Milano.

<sup>§</sup> Università di Modena e R.E..

<sup>||</sup> Università di Torino and INFN U.d.R. di Torino Università.

<sup>⊥</sup> Present address: ESRF, BP 220, F-38043 Grenoble Cedex, France.

- (1) Szostak, R. M. *Molecular Sieves*; Van Nostrand Reinhold: New York, 1989.
- (2) Meier, W. M.; Olson, D. H.; Baerlocher, Ch. *Atlas of Zeolite Structure Types*; Elsevier: London, 1996.
- (3) Thomas, J. M.; Bell, R. G.; Catlow, C. R. A. In *Handbook of Heterogeneous Catalysis*; Ertl, G., Knözinger, H., Weitkamp, J., Eds.; VCH: Weinheim, 1997; pp 286–310.
- (4) Kokotailo, G. T.; Lawton, S. L.; Olson, G. T.; Meier, W. M. *Nature* **1978**, *272*, 437.
- (5) Olson, G. T.; Kokotailo, G. T.; Lawton, S. L.; Meier, W. M. *J. Phys. Chem.* **1981**, *85*, 2238–2243.

(4) Taramasso, M.; Perego, G.; Notari, B. U.S. Patent No. 4,410,501, 1983.

(5) (a) Szostak, R.; Thomas, T. L. *J. Catal.* **1986**, *100*, 555. (b) Szostak, R.; Nair, V.; Thomas, T. L. *J. Chem. Soc., Faraday Trans. 1* **1987**, *83*, 487–494.

(6) Sulikowski, B. *Heterog. Chem. Rev.* **1996**, *3*, 203–268.

topology<sup>9</sup> makes this structure of relevance also in the mineralogical field.

In recent years, TS-1 and Fe-MFI have attracted particular interest in the scientific community as partial oxidation catalysts. TS-1 is an active and selective catalyst in a number of low-temperature oxidation reactions with aqueous H<sub>2</sub>O<sub>2</sub> as the oxidant.<sup>10,11</sup> For this reason, it has been one of the most studied materials in heterogeneous catalysis in the last years.<sup>12–31</sup> As for Fe-MFI, one-step oxidation of benzene to phenol using N<sub>2</sub>O as oxidant<sup>32</sup> is worth noticing. Indeed, the selective addition of

an oxygen atom into an aromatic ring to yield phenols and naphthols is a very promising tool for the chemical industry, because the commonly employed route via the three-step cumene process is of great technological complexity. As was the case for TS-1, also Fe-MFI samples have been subjected to a number of investigations.<sup>33–38</sup>

Template burning (or calcinations) of the as synthesized material is a key step in the activation of a zeolitic material for its application as a catalyst or as a membrane. Several studies have been performed to optimize the heating strategy adopted for the template removal<sup>48–50</sup> and to try to activate microporous and mesoporous materials, under mild conditions.<sup>39</sup>

The template removal process in MFI zeolites has been investigated by different techniques,<sup>40–54</sup> the most employed being thermal gravimetric analysis (TGA),<sup>40–45,54</sup> eventually

- (7) Flanigen, E. M.; Bennett, J. M.; Grose, R. W.; Cohen, J. P.; Patton, R. L. M.; Kirchner, R.; Smith, J. V. *Nature* **1978**, *272*, 512.
- (8) Artioli, G.; Lamberti, C.; Marra, G. L. *Acta Crystallogr. B* **2000**, *56*, 2–10.
- (9) Vezzalini, G.; Quartieri, S.; Galli, E.; Alberti, A.; Cruciani, G.; Kvik, A. *Zeolites* **1997**, *19*, 323–325.
- (10) Notari, B. *Adv. Catal.* **1996**, *41*, 253–334 and references therein.
- (11) (a) Clerici, G. M.; Bellussi, G.; Romano, U. *J. Catal.* **1991**, *129*, 159–167. (b) Bellussi, G.; Carati, A.; Clerici, G. M.; Maddinelli, G.; Millini, R. *J. Catal.* **1992**, *133*, 220–230. (c) Mantegazza, M. A.; Leofanti, G.; Petrini, G.; Padovan, M.; Zecchina, A.; Bordiga, S. *Stud. Surf. Sci. Catal.* **1994**, *82*, 541–550. (d) Mantegazza, M. A.; Petrini, G.; Spanò, G.; Bagatin, R.; Rivetti, F. *J. Mol. Catal. A* **1999**, *146*, 223–228.
- (12) (a) Millini, R.; Previti Massara, E.; Perego, G.; Bellussi, G. *J. Catal.* **1992**, *137*, 497–503. (b) Lamberti, C.; Bordiga, S.; Zecchina, A.; Carati, A.; Fitch, A. N.; Artioli, G.; Petrini, G.; Salvalaggio, M.; Marra, G. L. *J. Catal.* **1999**, *183*, 222–231. (c) Marra, G. L.; Artioli, G.; Fitch, A. N.; Milanesio, M.; Lamberti, C. *Microporous Mesoporous Mater.* **2000**, *40*, 85–94.
- (13) (a) Hijar, C. A.; Jacobinas, R. M.; Eckert, J.; Henson, N. J.; Hay, P. J.; Ott, K. C. *J. Phys. Chem. B* **2000**, *104*, 12157–12164. (b) Henry, P. F.; Weller, M. T.; Wilson, C. C. *J. Phys. Chem. B* **2001**, *105*, 7452–7458. (c) Lamberti, C.; Bordiga, S.; Zecchina, A.; Artioli, G.; Marra, G. L.; Spanò, G. *J. Am. Chem. Soc.* **2001**, *123*, 2204–2212.
- (14) Tozzola, G.; Mantegazza, M. A.; Ranghino, G.; Petrini, G.; Bordiga, S.; Ricchiardi, G.; Lamberti, C.; Zulian, R.; Zecchina, A. *J. Catal.* **1998**, *179*, 64–71.
- (15) Deo, G.; Turek, A. M.; Wachs, I. E.; Huybrechts, D. R. C.; Jacobs, P. A. *Zeolites* **1993**, *13*, 365–373.
- (16) Huybrechts, D. R.; P. L. Buskens, P. L.; Jacobs, P. A. *J. Mol. Catal.* **1992**, *71*, 129–147.
- (17) (a) Scarano, D.; Zecchina, A.; Bordiga, S.; Geobaldo, F.; Spoto, G.; Petrini, G.; Leofanti, G.; Padovan, M.; Tozzola, G. *J. Chem. Soc., Faraday Trans.* **1993**, *89*, 4123–4130. (b) Li, C.; Xiong, G.; Xin, Q.; Liu, J.; Ying, P.; Feng, Z.; Li, J.; Yang, W.; Wang, Y.; Wang, G.; Liu, X.; Lin, M.; Wang, X.; Min, E. *Angew. Chem., Int. Ed.* **1999**, *38*, 2220–2222. (c) Ricchiardi, G.; Damin, A.; Bordiga, S.; Lamberti, C.; Spanò, G.; Rivetti, F.; Zecchina, A. *J. Am. Chem. Soc.* **2001**, *123*, 11409–11419. (d) Bordiga, S.; Damin, A.; Bonino, F.; Ricchiardi, G.; Lamberti, C.; Zecchina, A. *Angew. Chem., Int. Ed.* **2002**, *41*, 4734–4737.
- (18) (a) Bordiga, S.; Coluccia, S.; Lamberti, C.; Marchese, L.; Zecchina, A.; Boscherini, F.; Buffa, F.; Genoni, F.; Leofanti, G.; Petrini, G.; Vlaic, G. *J. Phys. Chem.* **1994**, *98*, 4125–4132. (b) Bordiga, S.; Boscherini, F.; Coluccia, S.; Genoni, F.; Lamberti, C.; Leofanti, G.; Marchese, L.; Petrini, G.; Vlaic, G.; Zecchina, A. *Catal. Lett.* **1994**, *26*, 195–208. (c) Lamberti, C.; Bordiga, S.; Arduino, D.; Zecchina, A.; Geobaldo, F.; Spanò, G.; Genoni, F.; Petrini, G.; Carati, A.; Villain, F.; Vlaic, G. *J. Phys. Chem. B* **1998**, *102*, 6382–6390. (d) Gleeson, D.; Sankar, G.; Catlow, C. R. A.; Thomas, J. M.; Spanò, G.; Bordiga, S.; Zecchina, A.; Lamberti, C. *Phys. Chem. Chem. Phys.* **2000**, *2*, 4812–4817.
- (19) (a) Zecchina, A.; Bordiga, S.; Lamberti, C.; Ricchiardi, G.; Scarano, D.; Petrini, G.; Leofanti, G.; Mantegazza, M. *Catal. Today* **1996**, *32*, 97–106.
- (20) Trong On, D.; Le Noc, L.; Bonnevot, L. *Chem. Commun.* **1996**, 299–300.
- (21) (a) Bolis, V.; Bordiga, S.; Lamberti, C.; Zecchina, A.; Petrini, G.; Rivetti, F.; Spanò, G. *Langmuir* **1999**, *15*, 5753–5764. (b) Bolis, V.; Bordiga, S.; Lamberti, C.; Zecchina, A.; Petrini, G.; Rivetti, F.; Spanò, G. *Microporous Mesoporous Mater.* **1999**, *30*, 67–76.
- (22) (a) Millini, R.; Perego, G. *Gazz. Chim. Ital.* **1996**, *126*, 133–140. (b) Vayssilov, G. N. *Catal. Rev.—Sci. Eng.* **1997**, *39*, 209–251.
- (23) (a) Damin, A.; Bonino, F.; Ricchiardi, G.; Bordiga, S.; Zecchina, A.; Lamberti, C. *J. Phys. Chem. B* **2002**, *106*, 7524–7526. (b) Bordiga, S.; Damin, A.; Bonino, F.; Zecchina, A.; Spanò, G.; Rivetti, F.; Bolis, V.; Lamberti, C. *J. Phys. Chem. B* **2002**, *106*, 9892–9905. (c) Bonino, F.; Damin, A.; Bordiga, S.; Lamberti, C.; Zecchina, A. *Langmuir* **2003**, *19*, 2155–2161.
- (24) Millini, R.; Perego, G.; Seiti, K. *Stud. Surf. Sci. Catal.* **1994**, *84*, 2123–2129.
- (25) (a) Damin, A.; Bordiga, S.; Zecchina, A.; Lamberti, C. *J. Chem. Phys.* **2002**, *117*, 226–237. (b) Damin, A.; Bordiga, S.; Zecchina, A.; Doll, K.; Lamberti, C. *J. Chem. Phys.* **2003**, *118*, 10183–10194.
- (26) (a) de Man, A. J. M.; Sauer, J. *J. Phys. Chem.* **1996**, *100*, 5025–5034. (b) Ricchiardi, G.; de Man, A.; Sauer, J. *Phys. Chem. Chem. Phys.* **2000**, *2*, 2195–2204.
- (27) Sinclair, P. E.; Sankar, G.; Catlow, C. R. A.; Thomas, J. M.; Maschmeyer, T. *J. Phys. Chem. B* **1997**, *101*, 4232–4237.
- (28) Zicovich-Wilson, C. M.; Dovesi, R.; Corma, A. *J. Phys. Chem. B* **1999**, *103*, 988–994.
- (29) Sinclair, P. E.; Catlow, C. R. A. *J. Phys. Chem. B* **1999**, *103*, 1084–1095.
- (30) Munakata, H.; Oumi, Y.; Miyamoto, A. *J. Phys. Chem. B* **2001**, *105*, 3493–3501.
- (31) Vayssilov, G. N.; van Santen, R. A. *J. Catal.* **1998**, *175*, 170–174.
- (32) (a) Gubelmann, M.; Tirel, P.-J. Fr Patent. 2630735, 1988. (b) Kharitonov, A. S.; Alexandrova, T. N. L.; Vostrikova, A.; Ione, K. G.; Panov, G. I. Russ. Patent 4.445.646, 1988. (c) Meloni, D.; Monaci, R.; Solinas, V.; Berlier, G.; Bordiga, S.; Rossetti, I.; Oliva, C.; Forni, L. *J. Catal.* **2003**, *214*, 169–178.
- (33) (a) Sobolev, V. I.; Panov, G. I.; Kharitonov, A. S.; Romannikov, V. N.; Volodin, A. M.; Ione, K. G. *J. Catal.* **1993**, *139*, 435–443. (b) Dubkov, K. A.; Sobolev, V. I.; Panov, G. I. *Kinet. Catal.* **1998**, *39*, 72–79.
- (34) (a) Feng, X.; Hall, W. K. *J. Catal.* **1997**, *166*, 368–376. (b) Lewis, D. W.; Catlow, R. A.; Sankar, J.; Carr, S. W. *J. Phys. Chem.* **1995**, *99*, 2377–2383. (c) Chen, H.-Y.; Sachtler, W. M. H. *Catal. Today* **1998**, *42*, 73–83. (d) Joyner, R.; Stockenhuber, M. *J. Phys. Chem. B* **1999**, *103*, 5963–5976.
- (35) (a) Marturano, P.; Kogelbauer, A.; Prins, P. *J. Catal.* **2000**, *190*, 460–468. (b) Marturano, P.; Drozdová, L.; Kogelbauer, A.; Prins, R. *J. Catal.* **2000**, *192*, 236–247.
- (36) (a) Bordiga, S.; Buzzoni, R.; Geobaldo, F.; Lamberti, C.; Giamello, E.; Zecchina, A.; Leofanti, G.; Petrini, G.; Tozzola, G.; Vlaic, G. *J. Catal.* **1996**, *158*, 486–501. (b) Geobaldo, F.; Lamberti, C.; Bordiga, S.; Zecchina, A.; Turnes Palomino, G.; Otero Areán, C. *Catal. Lett.* **1996**, *42*, 25–33. (c) Berlier, G.; Spoto, G.; Bordiga, S.; Ricchiardi, G.; Fiescaro, P.; Zecchina, A.; Rossetti, I.; Selli, E.; Forni, L.; Giamello, E.; Lamberti, C. *J. Catal.* **2002**, *208*, 64–71. (d) Berlier, G.; Spoto, G.; Fiescaro, P.; Bordiga, S.; Zecchina, A.; Giamello, E.; Lamberti, C. *Microchem. J.* **2002**, *71*, 101–116.
- (37) (a) Spoto, G.; Zecchina, A.; Berlier, G.; Bordiga, S.; Clerici, M. G.; Basini, L.; *J. Mol. Catal. A* **2000**, *158*, 107–114. (b) Ferretti, A. M.; Oliva, C.; Forni, L.; Berlier, G.; Zecchina, A.; Lamberti, C. *J. Catal.* **2002**, *208*, 83–88. (c) Berlier, G.; Spoto, G.; Bordiga, S.; Ricchiardi, G.; Fiescaro, P.; Zecchina, A. *J. Mol. Catal. A* **2002**, *182/183*, 359–366. (d) Berlier, G.; Zecchina, A.; Spoto, G.; Ricchiardi, G.; Bordiga, S.; Lamberti, C. *J. Catal.* **2003**, *215*, 264–270. (e) Berlier, G.; Bonino, F.; Zecchina, A.; Bordiga, S.; Lamberti, C. *ChemPhysChem* **2003**, *4*, 1073–1078.
- (38) Milanesio, M.; Lamberti, C.; Aiello, R.; Testa, F.; Piana, M.; Viterbo, D. *J. Phys. Chem. B* **2000**, *104*, 9951–9953.
- (39) (a) Méhn, D.; Kónya, Z.; Halász, J.; Nagy, J. B.; Rác, B.; Molnár, A.; Kiricsi, I. *Appl. Catal., A* **2002**, *232*, 67. (b) Meretei, E.; Halász, J.; Méhn, D.; Kónya, Z.; Korányi, T. I.; Nagy, J. B.; Kiricsi, I. *J. Mol. Struct.* **2003**, *651*–653, 323–330.
- (40) Romannikov, V. N.; Mastikhin, V. M.; Hočevár, S.; Črňaj, B. *Zeolites* **1982**, *3*, 311–320.
- (41) Parker, L. M.; Bibby, D. M.; Patterson, J. E. *Zeolites* **1984**, *4*, 168–174.
- (42) Souillard, M.; Bilger, S.; Kessler, H.; Guth, J. L. *Zeolites* **1987**, *7*, 463–470.
- (43) Souillard, M.; Bilger, S.; Kessler, H.; Guth, J. L. *Thermochim. Acta* **1992**, *204*, 167–178.
- (44) Souillard, M.; Bilger, S.; Kessler, H.; Guth, J. L. *Zeolites* **1991**, *11*, 107–115.
- (45) Bilger, S.; Souillard, M.; Kessler, H.; Guth, J. L. *Zeolites* **1991**, *11*, 784–791.
- (46) Nowotny, M.; Lercher, J. A.; Kessler, H. *Zeolites* **1991**, *11*, 454–459.
- (47) Ajot, H.; Russmann, C.; Joly, J. F.; Kessler, H. *Stud. Surf. Sci. Catal.* **1994**, *87*, 477–485.
- (48) Geus, E. R.; van Bekkum, H. *Zeolites* **1995**, *15*, 333–341.
- (49) den Exter, M. J.; van Bekkum, H.; Rijn, C. J. M.; Kapteijn, F.; Moulijn, J. A.; Schellevis, H.; Beenakker, C. I. N. *Zeolites* **1997**, *19*, 13–20.
- (50) Dong, J.; Lin, Y. S.; Hu, M. Z.-C.; Peascoe, R. A.; Payzant, E. P. *Microporous Mesoporous Mater.* **2000**, *34*, 241–253.
- (51) Pachtová, O.; Kocirik, M.; Bernauer, B.; Bauer, F. *Stud. Surf. Sci. Catal.* **2002**, *142*, 303–310.
- (52) Jirka, I.; Pachtová, O.; Novák, P.; Kocirik, M. *Langmuir* **2002**, *18*, 1702–1706.
- (53) Pachtová, O.; Kocirik, M.; Zikánová, A.; Bernauer, B.; Miachon, S.; Dalmon, J.-A. *Microporous Mesoporous Mater.* **2002**, *55*, 285–296.

coupled with the in situ analysis of the evolved volatile products by mass spectroscopy or gas chromatographic techniques.<sup>41,43,45</sup> Other studies involve IR,<sup>44,46</sup> <sup>13</sup>C MAS,<sup>44,54</sup> and <sup>29</sup>Si MAS NMR,<sup>54</sup> and XRD<sup>48–53</sup> techniques. The latter was applied under ex situ conditions, by extracting the sample at different stages of the calcination reaction, or under partial in situ conditions, by acquiring only few selected reflections.

In this work, we report the first XRD study on template burning of TS-1 and Fe-MFI zeolites performed under in situ conditions by increasing the sample temperature, in oxygen flow, in the 300–1000 K range. This experiment allowed a thorough investigation of the structural rearrangements induced by the template burning on the zeolitic framework. Also, a detailed kinetic analysis was performed to obtain the apparent activation energy ( $E_a$ ) of the template burning process in Fe-MFI and TS-1, employing the procedure described by Kennedy and Clark<sup>55</sup> for nonisothermal data. For TS-1 only, the template burning reaction has been studied also under isothermal conditions at four different temperatures to perform the kinetic analysis, employing the general Avrami model,<sup>56</sup> to obtain the activation energy of the process through the corresponding Arrhenius plot. As was the cases of previously investigated solid-phase transitions,<sup>57–59</sup> the high X-ray flux available at the third generation synchrotron radiation sources, like the ESRF, and the use of a suitably designed area detector setup have been two mandatory points allowing us to follow in real time the template burning process.

An attempt to follow the template removal inside zeolites by diffraction techniques has been reported by Muncaster et al.<sup>60</sup> The authors reported a synchrotron radiation single-crystal XRD study of the template decomposition inside CoAPO-44 and DAF-1 zeolites, performed by collecting five static data sets at the following five temperatures: 150, 273, 473, 673, 773 K. No kinetic analysis can be performed in such conditions. Our approach, based on a powder diffraction experiment, can be applied to almost all zeolitic systems, in particular to the microcrystalline systems employed in the real industrial applications.

## 2. Experimental and Methods

**2.1. Synthesis and Preliminary Characterization.** A TS-1 sample has been synthesized in EniChem (now *Polimeri Europa*) laboratories following a procedure described in the original patent.<sup>4</sup> Absence of extraframework TiO<sub>2</sub> particles has been proved by UV–vis and XANES spectroscopies and by the absence of the 144 cm<sup>−1</sup> Raman band.<sup>17c</sup> Thermal gravimetric analysis (TGA) was carried out employing a TGA/SDTA851 Mettler Toledo instrument under the same conditions adopted in the XRPD experiment. Fe-MFI sample was prepared following the

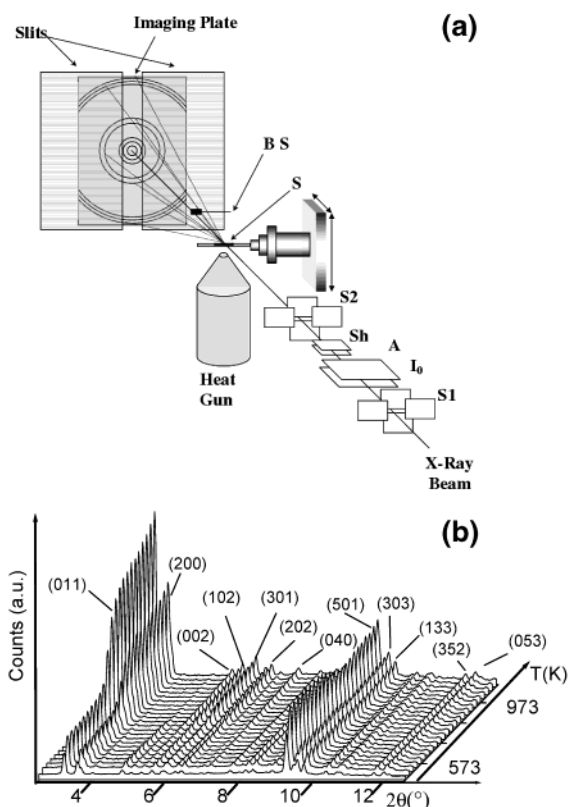


**Figure 1.** (a) Diagram of the in situ experimental setup (adapted from ref 63). See text for the labels. (b) Evolution of the XRPD patterns in the 2.5°–12.5°  $2\theta$  interval (corresponding to 14.2–2.8 Å  $d$  spacing) as a function of the temperature during the in situ template burning. Main reflections have been indicated. Because of the similar length of the  $a$  and  $b$  axes, ( $hkl$ ) and ( $khl$ ) reflections show severe overlapping, so that, for example, (011) and (101) contribute to the same peak, and only the strongest peak is indicated in the picture.

method of Szostak et al.<sup>5</sup> Absence of extraframework Fe atoms, before calcination, was checked by EXAFS and XANES spectroscopies.<sup>36c,d</sup> On both samples, preliminary XRPD experiments were carried out ex situ, before and after calcinations, to check the sample quality and absence of other phases, on a laboratory Bruker D5005 instrument equipped with Göbel mirrors.

**2.2. In Situ XRPD Setup.** In situ time-resolved XRPD template burning experiments were performed at the European Synchrotron Radiation Facility (ESRF), BM08 (GILDA) beam line,<sup>61</sup> within the public user program.<sup>62</sup> Figure 1a reports a scheme of the adopted XRPD setup. The GILDA focusing optics provide a beam spot of about 2 (horizontal)  $\times$  1 (vertical) mm<sup>2</sup> at the sample position (S). The resolution slit system (vertical and horizontal) (S1) defines the effective spot size with a resolution of  $\pm 0.25$   $\mu$ m. The ionization chamber I<sub>0</sub>, placed after the S1 slits, monitors the effective photon flux on the sample. The absorber (A) has not been used in this experiment since no peak saturation problems occurred. A further slit system (S2) has been placed just before the sample (S) to reduce the air scattering background. Finally, a beam stopper (BS) prevents the direct beam from reaching the detector, which was a flat Fuji 200 400 mm<sup>2</sup> image plate (IP) supported by a magnetic plate. The sample-to-IP distance was set to a nominal distance of 330 mm and then calibrated to 329.58 mm using the standard procedure. The two slits in front of the IP have been set with an opening of 3 mm aligned to the X-ray beam. The IP support is mounted on a computer controlled, high precision translating stage,

(54) El Hage-Al Asswad, J.; Dewaele, N.; Nagy, J. B.; Hubert, R. A.; Gabelica, Z.; Derouane, E. G.; Crea, F.; Aiello, R.; Nastro, A. *Zeolites* **1988**, 8, 221–227.

(55) Kennedy, G. A.; Clark, S. M. *Thermochim. Acta* **1997**, 307, 27–35.

(56) Hancock, J. D.; Sharp, J. H. *J. Am. Ceram. Soc.* **1972**, 55, 74–77.

(57) Shido, T.; Prins, R. *Curr. Opin. Solid State Mater. Sci.* **1998**, 3, 330–335 and references therein.

(58) Bellotto, M.; Gualtieri, A.; Artioli, G.; Clark, S. M. *Phys. Chem. Miner.* **1995**, 22, 207–214.

(59) (a) Norby, P. *J. Am. Chem. Soc.* **1997**, 119, 5215–5221. (b) Grey, C. P.; Poshni, F. I.; Gualtieri, A. F.; Norby, P.; Hanson, J. C.; Corbin, D. R. *J. Am. Chem. Soc.* **1997**, 119, 1981–1989. (c) Gualtieri, A. F.; Norby, P.; Artioli, G.; Hanson, J. C. *Microporous Mater.* **1997**, 9, 189–201. (d) Gualtieri, A. F.; Norby, P.; Artioli, G.; Hanson, J. C. *Phys. Chem. Miner.* **1997**, 24, 191–199. Norby, P.; Poshni, F. I.; Gualtieri, A. F.; Hanson, J. C.; Grey, C. P. *J. Phys. Chem. B*, **1998**, 102, 839–856.

(60) Muncaster, G.; Sankar, G.; Catlow, C. R. A.; Thomas, J. M.; Bell, R. G.; Wright, P. A.; Coles, S.; Teat, S. J.; Clegg, W.; Reeve, W. *Chem. Mater.* **1999**, 11, 158–163.

(61) [http://www.esrf.fr/exp\\_facilities/BM8/handbook/control.html](http://www.esrf.fr/exp_facilities/BM8/handbook/control.html)

(62) Artioli, G.; Lamberti, C.; Marra, G. L. ESRF Proposal CH-687.



moving along  $x$ . A more detailed description of the instrumentation and experimental setup can be found elsewhere.<sup>63</sup>

The thermal treatments were carried out using a Cyberstar gas blower, controlled by a Eurotherm 902b temperature controller, positioned in proximity of the central part of the capillary (Heat Gun in Figure 1a). The temperature was monitored by a thermocouple inserted at the gun opening, and the real temperature of the capillary was calibrated by monitoring, in a parallel experiment, the cell volume expansion (obtained by Rietveld analysis) of a silver wire from 300 to 1000 K. Zeolite powder was ground and carefully packed in an open 0.7 mm quartz capillary having glass wool bundles to stop the powder dispersion and, at the same time, to allow the oxygen flux ( $\sim 1.1$  bar) required for the template burning. The capillary was then mounted employing a ferrule on a T-piece and inserted on a goniometer head, to allow the application of the  $O_2$  flux through the capillary and simultaneous sample oscillation. For the isotherm experiments, given the small mass of the capillary, the set temperature was reached within a few seconds after the start of the experiment by translating the gas blower on the sample.

**2.3. Data Collection and Analysis.** All data were collected using a wavelength of 0.826 67(6) Å, calibrated against the lattice parameters of the NIST  $LaB_6$  standard (SRM 660b; nominal  $a = 4.156\ 95(6)$  Å at rt). X-ray diffraction patterns were accumulated on the IP detector, using the translating system described above (Figure 1a). A continuous set of diffraction patterns have been obtained with this procedure as a function of time. The time resolution for each experiment was defined by the translation speed of the IP detector combined with the slit width opening. The images collected on the IP were retrieved using a Fuji BAS2500 scanner. Conventional intensity versus  $2\theta$  files were obtained by pixel integration of the image using a flexible software especially developed for this purpose. For a zoom in the  $2.5^\circ$ – $12^\circ$   $2\theta$  region of the obtained XRPD patterns, see Figure 1b, where the changes induced by template removal are evident. The large intensity increase of the (011) and (200) reflections upon increasing the temperature are worth noting. This is the fingerprint of the progressive reduction of the electron density due to the presence of molecules inside the channels, showing long range order. A similar, although not so spectacular, behavior is observed for the reflections around  $2\theta = 6^\circ$  and for the (040) reflection. The reflections in the  $2\theta = 9^\circ$ – $10^\circ$  region, related to the zeolite framework, undergo much smaller variations. The sharpening of the low angle peaks is likely due to the removal of disordered template species.

At first, for both TS-1 and Fe-MFI, nonisothermal runs were carried out, using a temperature ramp of 7.2 K/min from 300 to 1000 K and by recording the XRPD spectra up to  $(\sin \theta)/\lambda = 0.56$ . These experiments allowed the identification of the temperature region, where the template decomposition occurs. Four isothermal runs were collected on TS-1 at four different temperatures (658, 669, 684, 701 K). Under the adopted experimental conditions, from every run, the scanned image produced about 45 integrated powder patterns as a function of time or temperature. The powder patterns were then individually refined with GSAS.<sup>64</sup> The structural model of the zeolite framework and the positions of the atoms of the molecules in the channels were taken from the literature. The tetrapropylammonium ion ( $TPA^+$ ) disordered model was derived from a detailed single-crystal study performed on different metal substituted MFI zeolites by some of us from data collected at ID11 beamline of the ESRF.<sup>65</sup> The site occupancy fractions of the atoms of the  $TPA^+$  ions were constrained and adapted to the molecular disorder

model, therefore, reducing the number of parameters refined. The evolution of the template decomposition reaction was deduced by the variation of the refined overall template occupancy factor  $X_{TPA}$ ,<sup>66</sup> which was transformed into the corresponding conversion value  $\alpha$  defined as:<sup>67</sup>

$$\alpha(T, t) = 1 - X_{TPA}(T, t) \quad (1)$$

where  $T$  and  $t$  are the temperature and the time, respectively. Kinetic analysis was performed on the  $\alpha$  versus  $t$  isothermal data employing the procedure described by Hancock and Sharp,<sup>56</sup> while the  $\alpha$  versus  $T$  nonisothermal data were analyzed with the method reported by Kennedy and Clark,<sup>55</sup> as described in detail in the 3.2 section.

### 3. Results and Discussion

This chapter is divided into two parts. Section 3.1 is devoted to the analysis of the evolution of the structural parameters during the nonisothermal calcinations. Section 3.2 describes the results of the kinetic analysis and the corresponding kinetic model for template removal.

**3.1. Evolution of the Structural Parameters during the Calcinations in Temperature Ramp.** In this section, we describe the evolution of the most important structural parameters obtained by the Rietveld refinement of XRPD data collected on TS-1 and Fe-MFI during the calcination employing a heating ramp from rt up to 1000 K. Analogies and differences of the two systems are discussed. Section 3.1 is divided into three subsections. First, subsection 3.1.1 is devoted to establishing the evolution of the refined overall template occupancy factor  $X_{TPA}$  versus  $T$ . This allows us to define three important temperatures ( $T_s$ ,  $T_b$ , and  $T_f$ , corresponding to the start of the template decomposition, the start of the template burning, and the end of the template burning process, respectively) describing the key steps in the template burning process, which will be used to understand the evolution of the cell parameters (subsection 3.1.2) and of the atomic displacement parameters (ADP) of the Si atoms (subsection 3.1.3).

**3.1.1. Evolution of Template Occupancy Factor.** Figure 2a reports the direct comparison between the data collected by conventional TGA (continuous line, left axis) and by in situ XRPD (solid squares, right axis) during the template burning in TS-1. For TGA, we report as usual the percent loss of weight, while, for XRPD, we report the refined  $X_{TPA}$ <sup>67</sup> factor. It is worth recalling that the two techniques monitor two different physical quantities: the overall amount of material leaving the sample, independently to its chemical nature and its previous order state,

(66) According to the synchrotron radiation single-crystal study reported in ref 65 and to previous ones quoted therein, two positions have been found for the template molecule, hereafter labeled as  $TPA_1$  and  $TPA_2$ , showing an occupancy of 0.6 and 0.4, respectively. The position of the N atom is the same for both components. For all the atoms of each component (1 N and 9 C atoms), only one unique site occupancy factor (SOF) has been refined according to the following constraints:  $X_{TPA} = SOF(N) = SOF(C_1)/0.6 = SOF(C_2)/0.4$  ( $j$  running over the 9 C atoms of each TPA molecule). In this way, the electron density of the two components is modeled using a unique independent parameter, which gives directly the value of  $X_{TPA} = SOF(N)$ . Note that the relative weights of 0.6 and 0.4 for  $TPA_1$  and  $TPA_2$  have been refined by a trial and error method. Technically speaking, the "FRAC" variables were constrained, employing the "set atomic parameter constraints" menu in the GSAS software.

(67) For both TS-1 and Fe-MFI samples, measured at room temperature before template burning, the refined  $X_{TPA}$  factor was 1.21. This is a clear consequence of the correlation between occupancy and ADP factors. Occupancy factors greater than unit have no physical meaning. Therefore, the values of  $X_{TPA}$  obtained at any  $T$  for both samples have been systematically rescaled by dividing by 1.21. Only rescaled values have been used to compute the conversion value  $\alpha(T)$  and to represent the data reported in Figure 2.

(63) (a) Meneghini, C.; Artioli, G.; Balerna, A.; Gualtieri, A. F.; Norby, P.; Mobilio, S. *J. Synchrotron Radiat.* **2001**, *8*, 1162–1166. (b) Martorana, A.; Deganello, G.; Longo, A.; Deganello, F.; Liotta, L.; Macaluso, A.; Pantaleo, G.; Balerna, A.; Meneghini, C.; Mobilio, S. *J. Synchrotron Radiat.* **2003**, *10*, 177–182.  
(64) Larson, A. C.; Von Dreele, R. B. *General Structure Analysis System (GSAS)*; Los Alamos National Lab. Report LAUR; 2000; pp 86–748 (<http://www.ccp14.ac.uk/solution/gsas/index.html>).  
(65) Palin, L.; Lamberti, C.; Kvick, A.; Testa, F.; Aiello, R.; Milanesio, M.; Viterbo, D. *J. Phys. Chem. B* **2003**, *107*, 4034–4042.

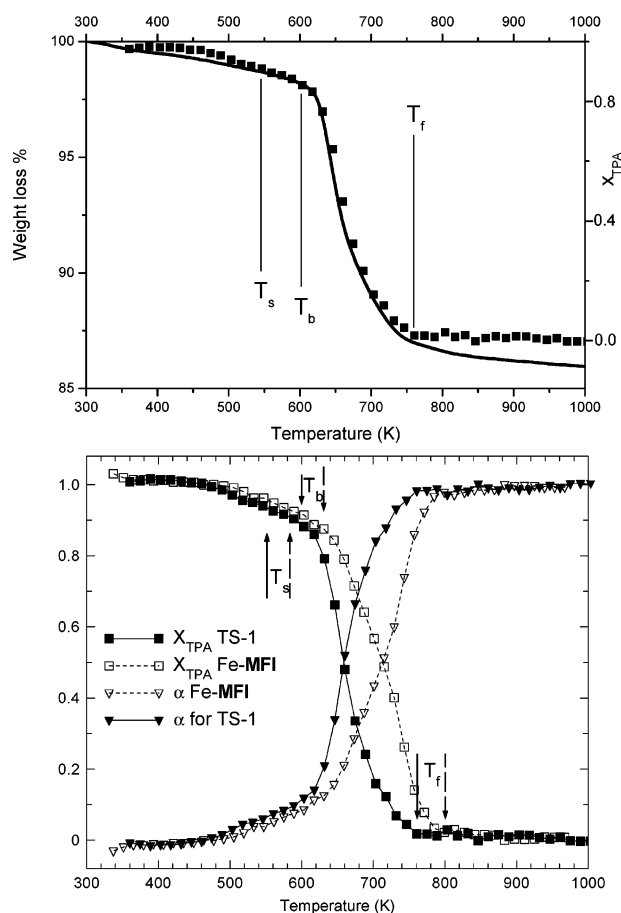


**Figure 2.** (a) Direct comparison between the refined TPA<sup>+</sup> occupancy factor (scattered squares, right axis) and the percent loss of weight (continuous line, left axis) during the template burning process inside TS-1. Vertical lines show the positions of  $T_s$ ,  $T_b$ , and  $T_f$  temperatures as defined in section 3.1. (b) Reaction coordinate  $\alpha$  for the TS-1 ( $\blacktriangledown$ ) and Fe-MFI ( $\nabla$ ), derived from the TPA<sup>+</sup> occupancy factor ( $X_{\text{TPA}}$ ), also shown as full and open squares for TS-1 and Fe-MFI, respectively (the esd's on  $\alpha$  are almost constant and equal to 2 on the second digit; they are not shown in the picture for clarity). Vertical arrows show the positions of  $T_s$ ,  $T_b$ , and  $T_f$  temperatures (continuous and dashed for TS-1 and Fe-MFI, respectively).

and the electron density inside the zeolite pores due to material exhibiting long range order only. The agreement of the two curves reported in Figure 2a is impressive, and it testifies that the temperature calibration with the silver wire has been correctly performed. Furthermore, it shows that in situ time-resolved XRPD can retrieve all information obtained by TGA experiments in the template burning of zeolites, and on the top of this, it provides at any  $T$  (i.e., at any step of the reaction) the structural and crystallographic parameters.

Before entering into the discussion, let us define  $T_s$  and  $T_f$  as the temperatures where the refined value of the TPA occupancy ( $X_{\text{TPA}}$ ) starts to be, within the experimental error, lower than 1.0 and equal to 0.0, respectively, indicated by the vertical lines in Figure 2a. We shall also define  $T_b$  as the starting temperature of the template burning process, indicated by the sharp change in the slope of the  $X_{\text{TPA}}$  versus  $T$  curve.

For  $T_s < T < T_f$ , the agreement between TGA and XRPD data is remarkable. Conversely, for  $T < T_s$ , the TGA measures the desorption of physisorbed water molecules that cannot be observed by XRPD because of the disorder of the water molecules. Also for  $T > T_f$ , where the observed residual electron

density inside the zeolite channels is zero, TGA still shows sample loss. Two main phenomena cause the weight decrease in the  $T > T_f$  interval. (i) In the  $T_s < T < T_f$  range, the small fraction of template that has not evolved into volatile fragments has formed amorphous coke that is now burning at higher temperature. (ii) Silicon vacancies in the framework results in internal hydroxyl groups: at such high temperatures, framework rearrangements occur, by creation of new strained Si—O—Si bonds formed between two adjacent Si—OH groups by evacuation of one water molecule.<sup>8,68</sup>

The results obtained on both TS-1 and Fe-MFI systems are compared in Figure 2b, where both the refined  $X_{\text{TPA}}$  factor and the corresponding conversion value  $\alpha$  defined according to eq 1 are reported as a function of the temperature. The overall curve obtained for the Fe-MFI zeolite is shifted toward a higher  $T$  by about 30 K. This holds of course also for the three key temperatures previously defined, which are  $T_s = 550$  K (580 K),  $T_b = 600$  K (630 K), and  $T_f = 760$  K (800 K) for TS-1 (Fe-MFI). This temperature shift of the whole template burning reaction can be interpreted in terms of an additional electrostatic interaction between positively charged TPA<sup>+</sup> molecules and the zeolitic framework, which is more negatively charged when trivalent Fe(III) ions are present. It is worth noting that this interpretation is in keeping with the increased  $T_b$  observed with TGA measurements in ZSM-5 samples with increasing Al(III) content.<sup>40–42</sup>

**3.1.2. Evolution of the Cell Parameters.** Figure 3 reports the evolution of the cell volume and of the cell parameters of both TS-1 and Fe-MFI during the in situ thermal burning of the template in the 300–1000 K range. To allow a better comparison between the two systems and among the three cell parameters, we report adimensional values defined as  $V(T)/V_0$ ,  $a(T)/a_0$ ,  $b(T)/b_0$ , and  $c(T)/c_0$ , being the reference values those obtained in the refinement of the first recorded pattern ( $T = 350$  and 340 K for TS-1 and Fe-MFI, respectively). For both materials, we observe first an increase of the lattice parameters, indicating that the thermal expansion is the physical mechanism dominating this stage of the experiment. For  $T_s < T < T_b$ , the reaction starts with template decomposition, as indicated by the rather large volume expansion (see Figure 3a), even if the template elimination is not actually started, as stated by the small changes undergone by  $X_{\text{TPA}}$  in this range of  $T$ . The expansion trend stops at  $T_b$ , which is approximately 600 and 630 K for TS-1 and Fe-MFI, respectively (vide supra section 3.1.1). Above  $T_b$ , template burning starts and the cell volume and lattice parameters decrease. The difference of about 30 K in  $T_b$  values between TS-1 and Fe-MFI is observed in all parameters  $V(T)/V_0$ ,  $a(T)/a_0$ ,  $b(T)/b_0$ , and  $c(T)/c_0$ , being more visible in Figure 3a where the volumes are simultaneously reported. This difference does not hold for the starting stages of the process only but lasts for the whole template burning reaction, according to the observed variations in the  $X_{\text{TPA}}$  versus  $T$  curves (Figure 2b).

Despite the high final temperature (approximately 1000 K) reached at the end of the experiment, the unit cell contraction, due to template elimination, does not end in the collected data, probably because of the high speed of the temperature ramp (7.2 K/min) needed to carry out the experiment in a reasonable time. A longer experiment would result in a compression of the XRPD data on the image plate implying either a loss in

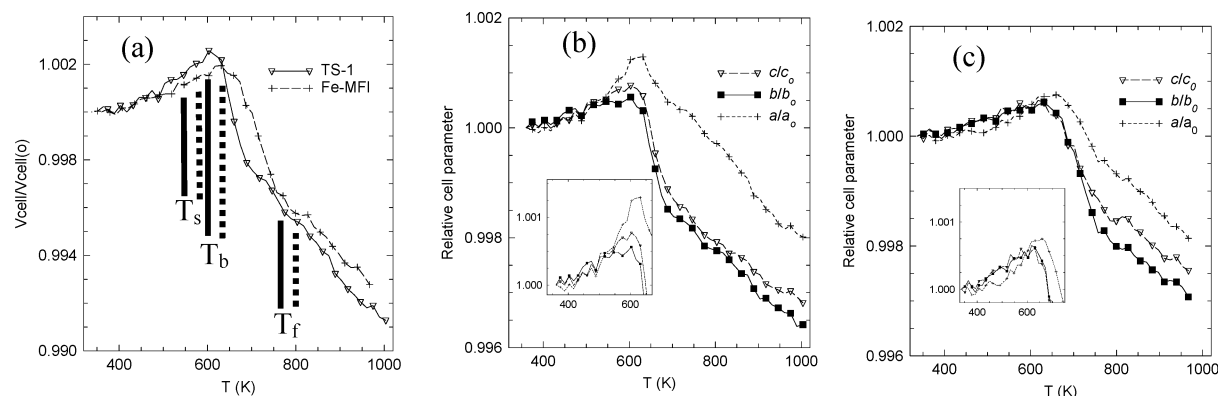


**Figure 3.** Evolution of the cell volume (a) and the lattice parameters for both TS-1 (b) and Fe-MFI (c) during the in situ template burning in the 300–1000 K range plotted as  $V(T)/V_0$ ,  $a(T)/a_0$ ,  $b(T)/b_0$ , and  $c(T)/c_0$  (being the reference values obtained at 350 and 340 K for TS-1 and Fe-MFI, respectively). Only the data corresponding to one over two refinements are reported for clarity (the esd's on the absolute value of the cell volume and lattice parameters are almost constant and are equal to 7 on the first decimal digit and 1 on the third decimal digit, respectively). In part a, vertical lines (continuous and dashed for TS-1 and Fe-MFI, respectively) show the positions of  $T_s$ ,  $T_b$ , and  $T_f$  temperatures (as defined in section 3.1).

temperature resolution or a loss in data statistics. In the temperature region where the template burning process has started, the slopes of the  $V(T)/V_0$ ,  $a(T)/a_0$ ,  $b(T)/b_0$ , and  $c(T)/c_0$  curves show a clear discontinuity at  $T = 770$  and  $800$  K for TS-1 and Fe-MFI, respectively. These values are very close to the temperature when the refined  $X_{\text{TPA}}$  goes to zero (being  $T_f = 760$  and  $800$  K for TS-1 and Fe-MFI, respectively). This means that the small change in the slopes of  $V(T)/V_0$ ,  $a(T)/a_0$ ,  $b(T)/b_0$ , and  $c(T)/c_0$  curves reflects the change in the physical process occurring within the zeolite. Between  $T_b$  and  $T_f$ , the driving process is the evolution of ordered molecules into volatile fragments which are evacuated from the zeolite channels. At  $T$  values higher than  $T_f$ , the prevalent processes are the elimination of amorphous coke and the condensation of Si–O–Si bridges at defective sites.

According to parts b and c of Figure 3, it is evident that, for  $T < T_s$  ( $T_s = 550$  and  $580$  K for TS-1 and Fe-MFI, respectively), the volume increase due to thermal expansion is isotropic for both samples within the experimental error. Between  $T_s$  and  $T_b$ , however, the observed volume increase is very anisotropic (see enlarged inset), the  $a$  axis having a substantially larger coefficient of thermal expansion. This is related to the decomposition of the tetrapropylammonium ion into tripropylamine, propene, and a huge variety of secondary decomposition products, as already suggested by some authors.<sup>45,48</sup>

The anisotropy holds during the volume contraction too. At this stage, we observe the effects of the expulsion of the secondary products outside the pores. During the whole process ( $T > T_b$ ), for both TS-1 and Fe-MFI, the following inequalities hold:

$$a(T)/a_0 \gg c(T)/c_0 > b(T)/b_0 \text{ for } T > T_s \quad (2)$$

For TS-1 (Figure 3b), the  $a$  parameter exhibits a markedly different behavior with respect to  $b$  and  $c$  ( $b(T)/b_0 \approx c(T)/c_0$ ). At any given  $T > T_b$ , the relative contraction of the  $a$  parameter is  $\sim 40\%$  less pronounced<sup>69</sup> than for  $b$  and  $c$ . These results imply

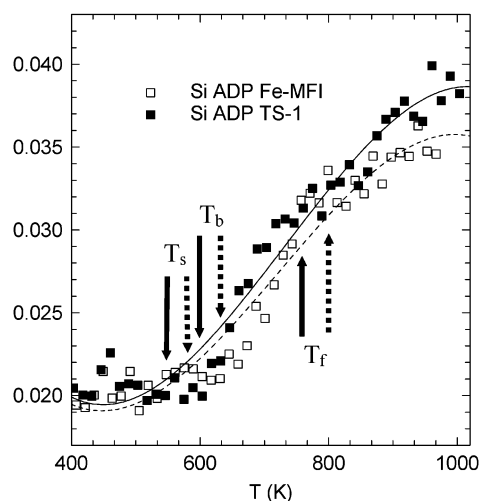


**Figure 4.** Si ADP, refined as a unique isotropic factor for all the 12 T sites, during the thermal treatment of a TS-1 (■) and Fe-MFI (□) samples. Full and dashed curves represent the cubic interpolation of TS-1 and Fe-MFI data, respectively (the esd's on ADP are almost constant and equal to 1 on the third decimal digit; they are shown in the picture for clarity). Vertical arrows show the positions of  $T_s$ ,  $T_b$ , and  $T_f$  temperatures (continuous and dashed for TS-1 and Fe-MFI, respectively).

that, during the template burning process, the zeolite crystals are subjected to remarkable stress forces, which become dramatic when fast heating ramps are adopted. This strong anisotropic contraction certainly contributes to crack formation in zeolite crystals.<sup>48,49</sup>

For Fe-MFI (Figure 3c)  $b(T)/b_0$  is very close to  $c(T)/c_0$  up to  $720$  K. At higher temperatures, the difference in the  $b(T)/b_0$  values  $c(T)/c_0$  becomes greater than that observed for TS-1. Conversely, the differences in the relative contractions of  $a$  and  $b$  parameters<sup>69</sup> is less than 20% in this case. As was the case for TS-1, in the initial stages of the burning process ( $T_s < T < T_b$ ), an increase of  $a$  is observed.

**3.1.3. Evolution of the Si ADP Parameters.** The difference of approximately 30 K in the  $T_b$  values of TS-1 and Fe-MFI can also be appreciated in Figure 4, where the common Si ADP

(68) (a) Bordiga, S.; Roggero, I.; Ugliengo, P.; Zecchina, A.; Bolis, V.; Artioli, G.; Buzzoni, R.; Marra, G. L.; Rivetti, F.; Spanò, G.; Lamberti, C. *J. Chem. Soc., Dalton Trans.* **2000**, 3921–3929. (b) Bordiga, S.; Ugliengo, P.; Damin, A.; Lamberti, C.; Spoto, G.; Zecchina, A.; Spanò, G.; Buzzoni, R.; Dalloro, L.; Rivetti, F. *Top. Catal.* **2001**, *15*, 43–52. (c) Bolis, V.; Busco, C.; Bordiga, S.; Ugliengo, P.; Lamberti, C.; Zecchina, A. *Appl. Surf. Sci.* **2002**, *196*, 56–70.

(69) The value of 40% has been obtained by averaging over the 600–1000 K interval the normalized difference of the relative variation of  $a$  and  $b$  parameters, defined as  $\Delta_{ab}(T) = [a(T)/a_0 - b(T)/b_0]/[1 - (1/2)[a(T)/a_0 + b(T)/b_0]]$ .



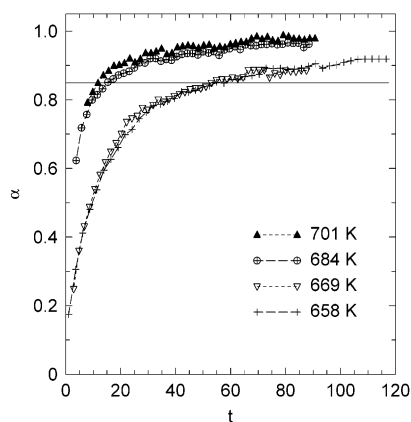


**Figure 5.** Reaction coordinate  $\alpha$  from eq 1 versus time (in minutes), for the isothermal treatment of TS-1 (the esd's on  $\alpha$  are almost constant and equal to 2 on the second digit; they are not shown in the picture for clarity).

(refined as unique isotropic factor for all the 12 T sites) is reported versus  $T$  for TS-1 and Fe-MFI (full and open squares respectively). Full and dashed curves represent the cubic interpolation of TS-1 and Fe-MFI data, respectively. Template burning causes a remarkable increase of the ADP of the Si atoms. The thermal origin of the ADP's increase is negligible, as witnessed by the almost constant behavior observed for  $T < T_s$ . Therefore, the phenomenon is ascribable mainly to an increase of disorder in the framework: (i) rupture of T–O–T bonds ( $T = \text{Si, Ti or Fe}$ ), (ii) heteroatom migration into partial or total extraframework positions (much more important in the Fe-MFI case<sup>36,70</sup>), (iii) shocks caused by the interactions of volatile molecules with the zeolitic walls.

**3.2. Kinetic Analysis.** The kinetic analysis of a chemical process leads to the interpretation of the mechanism of the reaction and to the estimation of the apparent activation energy.<sup>58,59</sup> Kinetic analysis was performed on the isothermal data employing the standard procedure described by Hancock and Sharp,<sup>56</sup> while the nonisothermal data were analyzed employing the method suggested by Kennedy and Clark.<sup>55</sup> Therefore, with the available data, we were able to compare the effect of the type of heteroatom (Fe or Ti) inserted in the MFI framework on the template burning process and to evaluate the different experimental procedure (isothermal or nonisothermal) employed to investigate the kinetic behavior of the TS-1 calcination process.

**3.2.1. Kinetic Analysis from in Situ Isothermal Calcinations of TS-1 Followed by XRPD.** The isothermal template burning experiment allowed us to perform the complete kinetic analysis of the reaction and to obtain a kinetic model for the template decomposition of TS-1. The four temperature values for the isothermal calcinations were chosen in the range 658–701 K to carry out the experiment in a reasonable time (less than 2 h) and, at the same time, to maintain an adequate time resolution of the process during data collection. For isothermal runs performed at  $T < 650$  K, a too large amount of unburned coke is formed.

Data from four isothermal calcinations at 658, 669, 684, and 701 K were collected, and the corresponding integrated XRPD patterns were analyzed by Rietveld refinement, as described previously (section 2.3), to obtain the conversion factors  $\alpha$

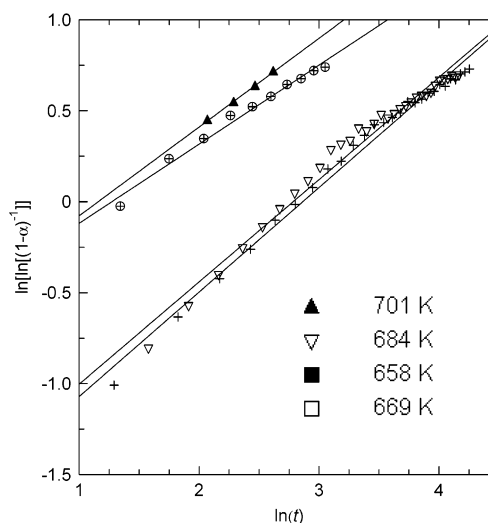


**Figure 6.** Determination of the reaction order, plotting  $\ln[-\ln(1 - \alpha)]$  vs  $\ln(t)$ , according to the Avrami law, for the isothermal calcinations of TS-1. Relative time ( $t$ ) is calculated as  $t/t_0$ , with  $t_0 = 1$  min). See section 3.2.1 for details.

versus  $t$ , calculated according to eq 1. The results are reported in Figure 5. XRPD data are incomplete in the first part of the reaction because of the time delay ( $\sim 2$  min) between gas blower positioning and X-ray shutter opening, imposed by the ESRF security procedure. This problem is negligible for the low  $T$  isotherms, where the reaction proceeds more slowly and is more important for the high  $T$  isotherms. Nevertheless the data are sufficient to carry out the kinetic analysis needed for the interpretation of the mechanism. The data analysis was performed following the standard procedure proposed by Hancock and Sharp,<sup>56</sup> employing a simple kinetic model described by the Avrami equation:

$$\alpha = 1 - \exp\{-(kt)^n\} \quad (3)$$

where  $k$  is the reaction constant,  $n$  is the reaction order, and  $t$  is the adimensionalized time.<sup>71</sup> By isolating the exponential on the right-hand term and by taking twice the logarithm of both terms, one obtains

$$\ln[\ln(1 - \alpha)^{-1}] = n \ln(t) + n \ln(k) \quad (4)$$

From the four sets of  $(\alpha, t)$  couples, one for each isothermal run, in Figure 6, we have plotted the left-hand term of eq 4 versus  $\ln(t)$ , obtaining the first indications on the kinetic behavior of the template burning reaction. The expected linear correlation between  $\ln[\ln(1 - \alpha)^{-1}]$  and  $\ln(t)$  is observed in the conversion range  $0.15 < \alpha < 0.85$ . Only the data obeying eq 4 are reported in Figure 6, being the only one from which  $n$  and  $k$  values can be extracted. The slope of the regression lines in Figure 6, fitted through the points of each isotherm, results in the value of  $n$  which is characteristic of the kinetic behavior of the reaction.<sup>72</sup> The left part of Table 1 (preliminary fit) reports the values of  $n$  and  $k$  for each isothermal run and the regression coefficients of the linear fit according to eq 4. The resulting  $n$  value, averaged over the four values obtained from each isotherm, is  $n = 0.51(2)$  (arithmetic mean). This value unambiguously

(70) Fejes, P.; Kiricsi, I.; Lazar, K.; Marsi, I.; Rockenbauer, A.; Korecz, L.; Nagy, J. B.; Aiello, R.; Testa, F. *Appl. Catal., A* **2003**, *242*, 247–266.

(71)  $t = t/t_0$  being  $t_0 = 1$  min.

(72) Bamford, C. H.; Tipper, C. F. *Comprehensive Chemical Kinetics*; Elsevier: New York, 1980; pp 41–113.



**Table 1.** Preliminary Fit, Values of the Reaction Order  $n$ , the Rate Constant  $k$ , and the Regression Coefficient  $r^2$ , Obtained by Fitting the Experimental Data Reported in Figure 6 According to Equation 4; Definitive Fit, Values of the Rate Constant  $k$  and of the Regression Coefficient  $r^2$  Obtained by Fitting the Same Data According to Equation 5, That Is, by Fixing  $n = 1/2$

$T$ (K)	preliminary fit			definitive fit with $n=1/2$	
	$n$	$k$	$r^2$	$k$	$r^2$
658	0.57(1)	0.057(5)	0.988	0.065(1)	0.984
669	0.55(1)	0.061(7)	0.979	0.069(1)	0.975
684	0.44(2)	0.28(5)	0.986	0.24(1)	0.964
701	0.49(1)	0.31(2)	0.999	0.30(1)	0.998

indicates that the rate-limiting step of the reaction is a diffusion process, with monodimensional advancement. A higher dimensional diffusion or different mechanism would imply higher  $n$  values, between 1.0 and 3.0 by moving from bi- to tridimensional reactions.<sup>57,72,73</sup> In fact, the obtained value ( $n = 0.51$ ) implies an instantaneous nucleation (zero order) or a deceleratory rate of nucleation of the reaction product. To reduce the degree of freedom of eq 4, we shall hereafter fix  $n = 0.5$ . Therefore, the best kinetic expression to fit the  $\alpha$  versus  $t$  data is

$$\ln[\ln(1 - \alpha)^{-1}] = \frac{1}{2} \ln(t) + \frac{1}{2} \ln(k) \quad (5)$$

Equation 5 allows the calculation of the rate constants  $k$  for each isothermal run; see right part of Table 1, definitive fit. The value of the obtained rate constants are then used in the plot of  $\ln(k)$  versus  $1/T$ , the logarithmic form of the Arrhenius equation:

$$k = Ae^{-E_a/RT} \quad (6)$$

where  $A$  is the frequency factor,  $E_a$  is the apparent activation energy of the process per unit mole,  $R = 8.314 \times 10^{-3} \text{ kJ mol}^{-1} \text{ K}^{-1}$  is the gas constant, and  $T$  is the absolute temperature. The Arrhenius plot for the template burning experiments is depicted in Figure 7. The resulting value of  $E_a$  is  $146 \pm 30 \text{ kJ/mol}$  with a regression coefficient of  $r^2 = 0.89$ .

Finally the isoconversional method of Friedman<sup>74</sup> has been applied to the present isothermal data to assess whether the investigated reaction is actually a multistep process. Unfortunately, only the  $0.6 < \alpha < 0.9$  range could be plotted and the result was only indicative. Notwithstanding, the absence of sharp changes in the curve slopes (apparent activation energies) tends to rule out a multistep reaction and support the one-step diffusion limited reaction model suggested by the obtained values of  $n$  reported in Table 1.

**3.2.2. Kinetic Analysis from in Situ Nonisothermal Calcinations Followed by XRPD.** Kennedy and Clark<sup>55</sup> reported that a single nonisothermal measurement (either from DSC or from in situ XRPD experiments) can be sufficient for a successful kinetic analysis. They demonstrated that the nonisothermal equivalent of the Arrhenius plot can be obtained employing the following equation:

$$\ln[b f(\alpha)/(T - T_0)] = \ln(A) - E_a/RT \quad (7)$$

where  $T$  is the absolute temperature,  $T_0$  is the temperature at

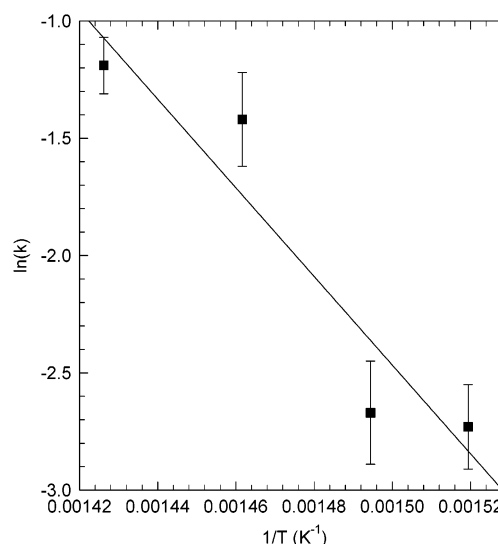


**Figure 7.** Arrhenius plot employing the  $\ln(k)$  values obtained from linear regression according to eq 5 (data from isothermal calcinations in Figure 5).

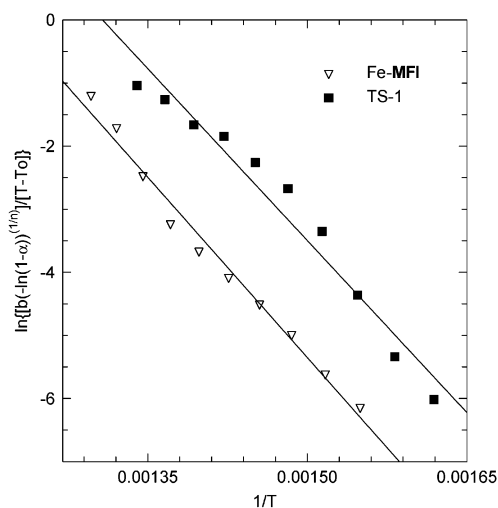


**Figure 8.** Arrhenius plot from linear regression of the data from the nonisothermal calcinations, employing eq 7 in the range  $0.13 < \alpha < 0.95$ .

the start of the reaction,  $b$  is the heating rate (given in K per the adimensionalized time  $t$ ), and  $f(\alpha)$  can be one of the possible rate equations proposed in the literature.<sup>75</sup> We employed the  $f(\alpha)$  corresponding to the Avrami equation<sup>75</sup> as already done for the isothermal calcinations:

$$f(\alpha) = [-\ln(1 - \alpha)]^{1/n} \quad (8)$$

where, as already stated in eq 3,  $n$  is the reaction order. Figure 8 shows the plot of the left-hand side of eq 7 versus  $1/T$ . From the slope of the curves, the apparent activation energy  $E_a$  has been obtained and reported in Table 2. The same table also reports the values employed for  $n$  and  $b$  in eq 7 and the corresponding regression coefficients. At first, it should be noted that the activation energies obtained for TS-1 from nonisothermal and isothermal data,  $151 \pm 11$  and  $146 \pm 30 \text{ kJ/mol}$ , respectively, are very similar. This confirms the findings of Kennedy and Clark<sup>55</sup> about the possibility of employing the

(73) Mazzuccato, E.; Artioli, G.; Gualtieri, A. *Phys. Chem. Miner.* **1999**, *26*, 375–381.

(74) Friedman, H. J. *Polym. Sci. C* **1964**, *6*, 183–195.

(75) See Table 1 in ref 55 for the possible expression for  $f(\alpha)$ , corresponding to the possible kinetic models.

**Table 2.** Values of the Reaction Order  $n$ , Heating Rate  $b$  (K per adimensionalized time  $t$ ), Temperature (K) at the Start of the Reaction  $T_0$ , Activation Energy  $E_a$  (kJ/mol), and the Regression Coefficient  $r^2$ , Obtained by Fitting the Nonisothermal Experimental Data Reported in Figure 8 According to Eq 7

	$n$	$b$	$T_0$	$E_a$	$r^2$
TS-1	0.5	7.2	550	$151 \pm 11$	0.961
Fe-MFI	0.45	7.2	580	$159 \pm 7$	0.985

nonisothermal data for a successful kinetic analysis. The remarkably lower error associated to the nonisothermal data is due to the much higher number of experimental points (all retrieved from the same nonisothermal experiment) used to perform the linear fit (compare Figures 7 and 8). The activation energy ( $159 \pm 7$  kJ/mol) for Fe-MFI, for which no isothermal data were available, can be obtained, confirming a very similar kinetic behavior with respect to TS-1.

**3.2.3. Kinetic Model for Template Decomposition.** The kinetic analysis indicates that the template decomposition reaction in TS-1 and in Fe-MFI is diffusion limited. In particular, the observed constant values of  $n \approx 0.5$  from the plot reported in Figure 6 (see section 3.2.1) demonstrate that the rate-limiting step is a diffusion process with monodimensional advancement.

We can infer that the elimination of the volatile products resulting from the template burning reaction is the physical phenomenon which can explain a diffusion-limited kinetic. MFI zeolites contain a two-dimensional system of interconnected channels, and it is rather surprising that a monodimensional reaction is observed. Nevertheless, channel shape and dimensions are different along the different crystallographic directions. A straight channel is present along the  $b$  axis, while a sinusoidal one can be found along the  $a$  axis. No connection is present along the  $c$  direction. We can infer that almost all material diffuses out through the straight  $b$  channel, and that sinusoidal channels are not an energetically convenient way for the diffusion of the gaseous products of the template burning reaction. This may be rationalized on the base of steric arguments, because the sinusoidal channels are longer and present a large number of adsorbing sites. Also, the average free path of the evolved molecular fragments is shorter in the sinusoidal channels than in the straight ones. The molecules diffusing in the sinusoidal channels therefore have a high probability of interaction with the framework and of back-reaction with other fragments to form larger moieties. Both mechanisms would effectively block the channels and prevent free diffusion of the molecules.

Recently, the formation of nanocavities (formed by multiple T–O–T ruptures) during the template removal has been reported.<sup>50,76</sup> The small dimensions of the crystallites ( $\sim 0.2$ – $0.4$   $\mu\text{m}$ ) should prevent the formation of this kind of defect in our samples. Anyway, these nanocavities should not be involved in the rate-determining step of the reaction (the evacuation of the evolved gas) since it would be hard to correlate the nanocavity formation with the observed diffusion limited kinetic, with monodimensional advancement of the template burning reaction.

This result confirms the findings of Patchova et al.<sup>53</sup> formulated by means of template removal experiments on large

silicalite crystals grown from fluoride media, monitored by light microscopy, nitrogen and iodine adsorption, and elemental analysis of N and C species eliminated during the thermal treatment. The large dimension and the perfect prismatic shape of the MFI crystals, employed in their experiments, allowed them a visual observation of the progress of the template removal reaction. The authors supposed that the template degradation products leave the crystal mainly by the straight channels.<sup>53</sup>

The anisotropy in the contraction of the lattice parameters in TS-1 during template burning (section 3.1.2 and Figure 2) is another strong indication of the presence of preferential directions in MFI crystal response to template burning. Although the lattice changes are a mixture of thermal expansion,  $\text{TPA}^+$  elimination, framework-extraframework molecule interaction, and structure relaxation, so that direct interpretation is difficult in the presence of multiple causes, it is evident that the small changes along the  $a$  lattice dimension is related to the preferential interaction of the molecules and the fragments within the sinusoidal channel along the  $a$  axis, during the  $\text{TPA}^+$  removal process. The MFI framework also supports different degrees of structure relaxation along different directions because of the anisotropic distribution of the structure building units.

Finally it is worth noting that the thermal treatment causes (i) the removal of the  $\text{TPA}^+$  molecule, (ii) the elimination of strained Si–O–Si bonds at defective sites, and (iii) the formation of additional defects. The formation of cracks and defects induced by the calcination process, observed for larger crystals by van Bekkum et al.,<sup>48</sup> is consistent with the changes observed in the refined average ADP parameter of the Si atoms.

## 4. Conclusions

The high quality of the XRPD data collected during isothermal and nonisothermal heat treatments allowed a careful investigation of the structural changes occurring during the template removal in the TS-1 and Fe-MFI samples and an exhaustive kinetic analysis of the template decomposition process. Concerning the structural parameters obtained after the Rietveld refinement, three main points deserve consideration. (i) The refined  $X_{\text{TPA}}$  versus  $T$  plot is very similar to the result of a TGA analysis (weight loss versus  $T$  plot), demonstrating the reliability of the experiment. Additionally to TGA, with this XRPD experiment, we obtained all the structural parameter variations occurring during the template burning. (ii) A clearly anisotropic variation of the unit cell parameters was observed, the  $a$  lattice parameter showing a significantly smaller decrease. (iii) The crystallinity of the sample decreases, probably because of the formations of defects, as shown by the increase observed in the  $T_b < T < T_f$  range for a common isotropic ADP parameter, employed in the refinement for the Si atoms.

For  $T_s < T < T_b$ , the reaction starts with template decomposition, as indicated by the rather large volume expansion (see Figure 3a) even if the template elimination is not yet started, as stated by the small changes undergone by  $X_{\text{TPA}}$  in this range of  $T$ . After this induction period, during which the template decomposition occurs, as suggested by some author,<sup>45,48</sup> the template burning starts. Kinetic analysis indicated that the template burning is a diffusion limited reaction with monodimensional advancement. The rate-limiting step of the reaction is the diffusion of the volatile products of the template burning

(76) Wegner, K.; Dong, J.; Lin, Y. S. *J. Membr. Sci.* **1999**, *158*, 17.

out of the crystal. Chemical and sterical considerations indicate that the straight channels along the *b* axis are the more favorable direction for the elimination of the template burning products.

These results are in keeping with the hypothesis proposed in the literature for template burning in **MFI** zeolites.<sup>48,51–53</sup> Also, the isothermal runs indicate that at low temperature there is an increased tendency to form amorphous and semiamorphous C-containing residues.

No significant difference is present between the TS-1 and the Fe-**MFI** samples as far as the fundamental reaction mechanisms are concerned. Nevertheless, the analysis of two differently substituted **MFI** samples (TS-1 and Fe-**MFI**) indicated that template removal temperature is affected by the type of heteroatom [Fe(III) or Ti(IV)] present in the framework. Indeed, in Fe-**MFI**, the whole reaction (see Figures 2–4) is moved to a higher temperature with respect to TS-1. This difference can be ascribed to the additional ionic forces existing in Fe-**MFI** for the formation of the ionic couples  $\text{FeO}_4^- - \text{TPA}^+$  with respect to the interaction (framework defect) $^- - \text{TPA}^+$ .

For TS-1, the Arrhenius plot yields an apparent activation energy of  $146 \pm 30$  and of  $151 \pm 11$  kJ mol $^{-1}$ , from isothermal and nonisothermal data, respectively ( $E_a = 159 \pm 7$  for Fe-**MFI** from nonisothermal data). No significant differences between isothermal and nonisothermal kinetic data were observed for the TS-1 sample, confirming the reliability of the used procedure for nonisothermal data. This approach, when applied to time-resolved XRPD studies, is much less time consuming (requesting, in principle, one single nonisothermal

run) with respect to the classic approach, which requires at least three isothermal runs. Fe-**MFI** shows the expected larger activation energy with respect to TS-1 ( $159 \pm 7$  versus  $151 \pm 11$ ), but we note that this difference is smaller than the experimental error.

**Acknowledgment.** This project was supported by MURST (Cofin 2000, Scienze Chimiche; Cofin 2001, Scienze della Terra). XRD measurements were performed at the BM8 GILDA beamline of the ESRF storage ring within the public user program. We are indebted to R. Buzzoni (PolimeriEuropa, Novara, Italy) for his help in the synthesis of the samples. L.P. acknowledges an INFM grant for his stay in Grenoble. M.M. acknowledges the “G. Donegani” foundation for a grant in 2001, when these data were collected and analyzed. The stimulating discussions with E. Mazzuccato (University of Modena e Reggio Emilia, Italy), G. Spanò and G. L. Marra (PolimeriEuropa, Novara, Italy), D. Viterbo (University of Piemonte Orientale), A. Longo (ISMN-CNR Palermo), and C. Prestipino, A. Zecchina, and S. Bordiga (University of Torino, Italy) are acknowledged. M.M. is grateful to M. Cavarero for continuous encouragement and support. We are indebted to the BM8 GILDA staff (in particular to C. Meneghini) and to R. Grizzetti (University of Milano, Italy) for their friendly and precious support during data collection. The constructive comments of the referees are acknowledged.

JA037229+